Soft Matter

PAPER

View Article Online
View Journal | View Issue

Check for updates

Cite this: *Soft Matter*, 2025, **21**, 6299

Co-motion of catalytic tubes and host droplets on superhydrophobic surfaces†

Amrutha S. V. and Oliver Steinbock *

Received 3rd June 2025,
Accepted 17th July 2025

DOI: 10.1039/d5sm00576k

rsc.li/soft-matter-journal

The ability to convert chemical energy into directed motion is a defining feature of living systems and a central goal in the design of synthetic active matter. Here, we report a self-propelling system in which a millimeter-sized tube is confined within a hydrogen peroxide droplet on a superhydrophobic surface. The tubes are synthesized *via* chemical garden self-assembly and catalyze the decomposition of the peroxide to water and oxygen gas. The resulting droplet-tube cell exhibits diverse dynamic behaviors, including propeller-like spinning, orbital rotation, and long-range translational jumps, driven by the asymmetric growth and bursting of internally generated gas bubbles. These motions are sensitive to hydrogen peroxide concentration, which governs both the internal gas production rate and the system's active lifetime. This system offers a simple yet versatile platform for exploring confined catalysis, emergent motility, and the design of soft, fuel-containing active materials.

Open Access Article. Published on 18 July 2025. Downloaded on 9/15/2025 10:13:04 AM.
This article is licensed under a Creative Commons Attribution 3.0 Unported Licence.

1. Introduction

The evolutionary emergence of active motion was a significant step that enabled living systems to seek food and energy sources as well as to escape predators. Cells employ various propulsion mechanisms, including flagella, cilia, and actin-based dynamic networks.[1–3] The latter not only drive locomotion but can also deform cells into highly elongated shapes.[4] The recent two decades have seen significant progress towards mimicking these types of reaction-driven, engine-free locomotion in chemical and other synthetic systems.[5–9]

Prominent examples include catalytic Janus particles[10–12] and Au/Pt nanorods,[13–15] which self-propel in hydrogen peroxide and similar solutions by generating chemical potential gradients or producing gas bubbles.[16,17] Catalytic microrockets[18] follow a similar principle but achieve propulsion through symmetry breaking, releasing bubbles preferentially from one end. These microtubes can be fabricated either by the spontaneous roll-up of vapor-deposited thin films or *via* electrochemical methods. To suppress bubble formation on their outer surfaces, the tubes are often coated with an insulating polymer layer (*e.g.*, polyaniline).[11]

Similar microrockets can also be produced by chemical self-assembly. Our group first demonstrated this by generating catalytically active tubes through precipitation reactions using the chemical-garden method.[19] Chemical gardens are hollow precipitate tubes that form when metal salt seeds are introduced into silicate or other solutions.[20–22] Tube lengths can reach several centimeters, with diameters ranging from about 10 μm to over 1 mm, depending on preparation conditions. These parameters are more easily controlled when the salt seed is replaced by a salt solution injected at constant rate and concentration.[23,24] The thin tube walls typically consist of metal hydroxides or oxides, but depending on the reagents, phosphates, carbonates, sulfides, and other materials can also form.[25–27] In silicate systems, the tubes additionally feature a very thin outer layer of amorphous silica.[28]

In 2021, Wang *et al.*[19] demonstrated that chemical garden tubes, formed by injecting Mn(II)/Cu(II) into sodium silicate solutions, can self-propel in hydrogen peroxide for over a day, reaching speeds of 5 mm s^{-1}. Each ejected bubble propels the tube forward by approximately one to two tube radii. The ejection frequency increases linearly with peroxide concentration, as revealed by acoustic detection of bursting bubbles. At lower H_2O_2 concentrations, this subsurface locomotion transitions into a vertical bobbing motion[29] and groups of tubes can exhibit collective dynamics.[30] While these studies focused on millimeter-scale tubes, micrometer-scale analogs can be fabricated by converting hollow $CaCO_3$ fibers into catalytic microrockets through shape-preserving chemical transformation.[31]

All of these examples differ fundamentally in one key aspect from the amoeboid motion of living cells:[32,33] their energy source is entirely external. In contrast, cells generate and store energy internally to power their movement. Here, we report a chemical system that mimics this biological feature by combining a cell-like, localized fuel reservoir with an internal chemical motor. The system consists of a millimeter-scale chemical

Department of Chemistry and Biochemistry, Florida State University, Tallahassee, FL 32306-4390, USA. E-mail: osteinbock@fsu.edu

† Electronic supplementary information (ESI) available. See DOI: https://doi.org/10.1039/d5sm00576k

Open Access Article. Published on 18 July 2025. Downloaded on 9/15/2025 10:13:04 AM.
This article is licensed under a Creative Commons Attribution 3.0 Unported Licence.

garden tube confined within a microliter-sized H_2O_2 droplet placed on a superhydrophobic surface.[34] We observe that the tubes are stationary, spinning, or rotating within the droplet. The drop volume increases intermittently due to internal gas bubble formation, and bubble bursting triggers repeated translational events of the synthetic cell over centimeter-scale distances.

2. Methods

2.1 Chemicals

Manganese chloride tetrahydrate ($MnCl_2{\cdot}4H_2O$, Fisher Chemical), copper sulfate pentahydrate ($CuSO_4{\cdot}5H_2O$, Fisher Chemical), sodium metasilicate pentahydrate ($Na_2SiO_3{\cdot}5H_2O$, Fisher Chemical), and hydrogen peroxide (30% v/v, VWR Chemicals) were used as received. All solutions were prepared using nanopure water (resistivity 18 MΩ cm) obtained from a Barnstead Easypure UV system.

2.2 Experimental methods

To produce the chemical garden tubes, we injected an aqueous solution containing 0.4 M $MnCl_2$ and 0.1 M $CuSO_4$ into a rectangular reservoir filled with 50 mL of 1.0 M sodium silicate solution (Fig. 1(a)).[19,35] The injection proceeded in the upward direction through a glass capillary (1.0 mm inner diameter) at a constant rate of 8.0 mL h^{-1}, controlled by a syringe pump (New Era Pump Systems, NE-4000). We stopped the injection once the precipitate tube reached the silicate solution surface. Subsequently, we extracted the precipitate tubes and rinsed them thoroughly with nanopure water. Chemical analyses of the tube material have been reported in ref. 19.

For self-propulsion experiments, we sectioned the hydrated tubes into 2 mm-long fragments using a syringe needle. We then placed each fragment on a 9 cm-diameter circular superhydrophobic surface, prepared by coating a polystyrene substrate with Rust-Oleum NeverWet spray (Rust-Oleum 275185; contact angle 165°).[36] Weight measurements of coated/uncoated substrates and an assumed dry film density of 0.3–0.5 g cm^{-3} yield an average layer height of 60–100 μm. Using a micropipette, we applied a 10 μL drop of hydrogen peroxide onto each fragment to initiate motion. This step sometimes required gentle positioning of the drop with the pipette tip as the drop moves freely over the water-repelling surface.

We captured the dynamics of the droplet-tube system with a digital camera (Nikon D3300) equipped with a 90 mm macro lens (Tamron) at a rate of 60 frames per s. To investigate the influence of hydrogen peroxide concentration on the propulsion behavior, we conducted systematic experiments across a range of concentrations. All experiments, including the tube production, were performed at room temperature.

2.3 Analysis

All video recordings were analyzed using custom MATLAB scripts developed in-house. Drop trajectories were smoothed using a low-pass Fast Fourier Transform (FFT) filter with a cut-off frequency of 1/3 Hz. For the instantaneous speed, cumulative distance, and drop area, we applied a median filter with a window size of 50 frames. Pixel-to-millimeter conversion was based on calibration measurements, yielding a factor of 0.070 mm per pixel.

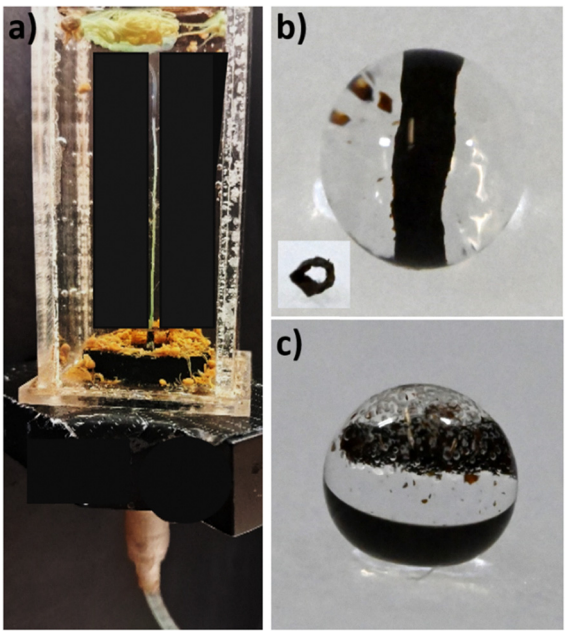

Fig. 1 Growth, physical structure, and confinement of chemical garden tubes in droplets. (a) Growth of a chemical garden tube inside a rectangular reactor containing 1 M sodium silicate solution. Injection is performed vertically through a glass capillary. Container width: 3 cm. (b) Top view of a 2 mm-long tube fragment in a 10 μL water droplet on a superhydrophobic surface. Inset: Axial view of the tube revealing its hollow interior. (c) Side view of a tube fragment suspended in a 10 μL droplet of 5% v/v H_2O_2.

3. Results and discussion

The presence of a superhydrophobic surface creates a nearly spherical drop shape. As shown in Fig. 1(b) and (c), the chemical garden tube is fully contained within the drop and does not protrude out of the liquid phase. The tube is hollow (inset of Fig. 1(b)) and has a rough internal surface texture that was characterized in ref. 19. Moreover, the active chemical garden tube is buoyant within the H_2O_2 drop and positions itself within the upper half of the drop. This buoyancy is due to trapped internal and attached external gas bubbles that result from the catalytic decomposition of H_2O_2 to H_2O and gaseous O_2. However, in water (Fig. 1(b)) or solutions with low H_2O_2 concentrations, the tube is positioned in the lower portion of the droplet.

3.1 Early stage dynamics

In the following, we will focus on the dynamics in droplets with an initial volume of 10 μL and an initial concentration of 15% v/v. Within the first few seconds of the experiment, the

 This journal is © The Royal Society of Chemistry 2025

Open Access Article. Published on 18 July 2025. Downloaded on 9/15/2025 10:13:04 AM.
This article is licensed under a Creative Commons Attribution 3.0 Unported Licence.

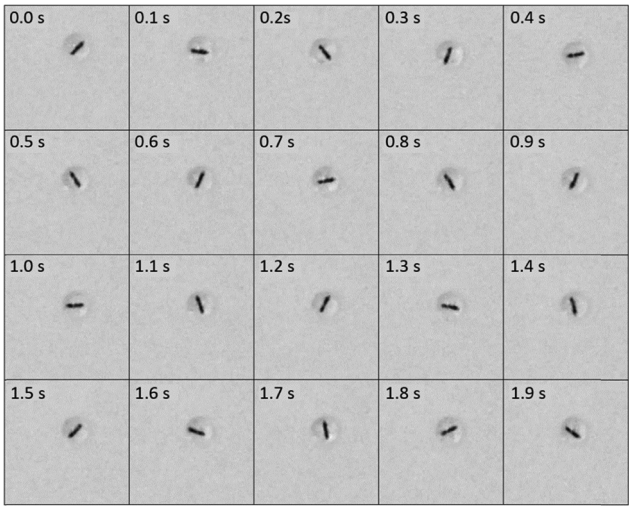

Fig. 2 Spinning motion of a chemical garden tube within a hydrogen peroxide droplet. A 2 mm-long tube continuously spins inside a 10 μL droplet of 15% v/v H_2O_2. The orientation of the tube changes steadily over time. The field of view is 1.4 × 1.4 cm^2, and the interval between consecutive frames is 0.1 s.

2-mm long tube undergoes a spinning motion within the droplet's upper hemisphere. A series of snapshots in Fig. 2 (shown here for the clockwise case) reveals that the tube completes one full rotation in about 0.6 s, while its geometric center remains essentially fixed in space. For shorter tubes (1 mm), spinning initiates with a back-and-forth motion along the tube axis and then stabilizes to spinning around a point closer to the tube's orifice.

The observed propeller-like spinning likely arises from torsional forces generated by the cyclic growth and detachment of O_2 bubbles from the tube's orifice. Each bubble pinch-off produces a tangential recoil force on the wall. Because the tube is tightly wedged at the droplet–air interface, these forces cannot translate the tube and instead sum to a net torque about its midpoint. Tiny asymmetries in the tube's overall cylindrical shape or in the shape of its orifices help to break the symmetry of bubble release, biasing the detachment sequence and choosing a typically consistent clockwise or counter-clockwise spin during the first seconds of the experiment.

An alternative explanation is that smaller bubbles detaching from the outside tube surface drag liquid upward and induce a compensating flow down the droplet's vertical axis, setting up recirculation cells that could shear the tubes and impart rotation. However, these vortex rolls are highly transient, likely decaying long before the next bubble forms. To slow down both the spinning motion and the rate of bubble release, we performed experiments in 5% v/v solutions. Here, the spinning motion that appears continuous at 15% v/v can be clearly resolved as individual steps, each advancing the tube by a few degrees. Each of these steps correlates to the observation of a single bubble that moves (within the top-down camera perspective) from the tube end to the droplet center (*i.e.* the drop's topmost point).

To confirm that inertial effects are small, the Reynolds number Re within the droplet was estimated using $Re = \rho UL/\mu$ with a characteristic length L = 2 mm, largest tip velocity U = 0.06 m s^{-1}, fluid density ρ = 1000 kg m^{-3}, and viscosity $\mu = 10^{-3}$ Pa s. The resulting value of Re ≈ 120 lies well below the onset of turbulence (Re ≈ 2000). Such lower Reynolds numbers indicate that viscous stresses dominate over inertia and that the flow remains laminar, consistent with the rapid damping of the stepwise rotations observed in 5% v/v H_2O_2 solutions.

Next we performed a closer analysis of the experiment in Fig. 2, yielding results that are representative for the dynamics during the first seconds of spinning tube motion. To extract the tube's orientation and position over time, we begin by building a static background image from the pixel-wise median values over the entire video and subtract this image from each grayscale frame to highlight moving features. A global intensity threshold then isolates dark regions and identifies the largest connected area as the tube. From this elongated region, we compute the centroid and principal-axis angle (reported between −90° and +90°) with the latter being unwrapped to remove jumps at the discontinuity, and then halved to recover the true orientation over time. Fig. 3(a) shows that the time-dependence of the original axis angle follows a saw-tooth-like curve for which two ''teeth'' correspond to a full spin cycle of the tube (red curve). The unwrapped angle (blue curve) steadily increases at about 10 rad s^{-1}, equivalent to 570 deg s^{-1} and a period of 0.63 s.

To track the droplet's position, we follow an analogous but polarity-reversed workflow. After building the same pixel-wise median background, each grayscale frame is subtracted and then positively thresholded to highlight the faint bright rim of the drop. Morphological closing removes spurious speckles, and the largest connected component within a fixed circular region-of-interest is taken as the droplet mask. We then extract the mask's centroid. By recording the centroid coordinates in each frame, we obtain the drop's trajectory over time (blue curve in Fig. 3(b)). For this experiment, we find that the droplet moved about 1 mm which is about 1/3 of its diameter. The trajectory of the tube's centroid matches this minute motion fairly closely which an offset of about 0.5 mm.

3.2 Late stage dynamics

Following the initial stage of propeller-like tube spinning in an essentially stationary solution drop, the dynamics of the system shifts to a new regime. Now, the oxygen bubbles burst less frequently and grow to larger sizes that greatly alter the effective size of the drop. A representative example is shown in Fig. 4 that illustrates the expanded drop, its collapse, and the resulting small, and essentially bubble-free, droplet. The bursting of these large bubbles is somewhat violent, often induces short-lived rapid bouncing, and can break off very small particles from the precipitate tube (see also Fig. 1(c)). We speculate that the accumulation of these fine, powder-like particles may contribute to the increased lifetime and size of the gas bubbles, as similar stabilization has been documented for Pickering

Open Access Article. Published on 18 July 2025. Downloaded on 9/15/2025 10:13:04 AM.
This article is licensed under a Creative Commons Attribution 3.0 Unported Licence.

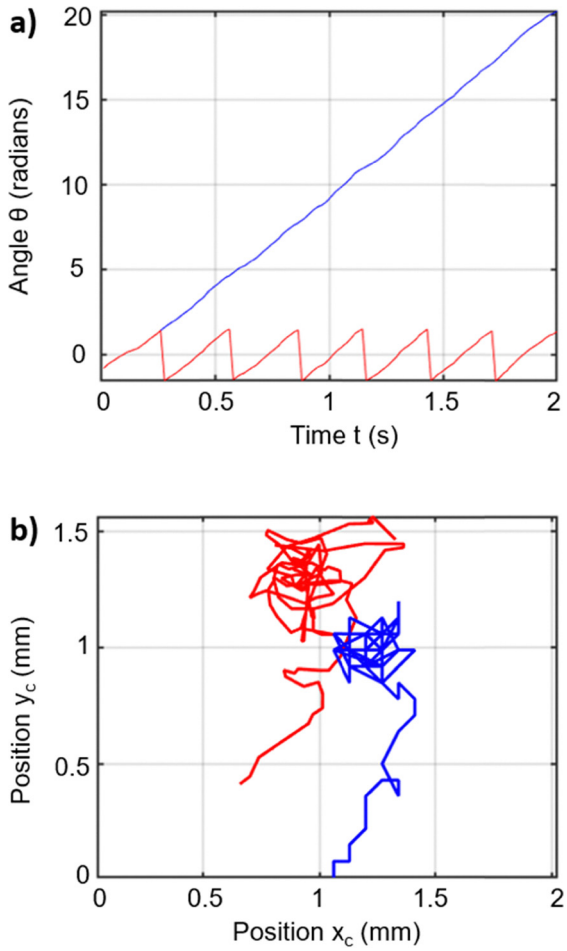

Fig. 3 Angular dynamics of a chemical garden tube and translational trajectories. (a) Time evolution of the tube's orientation angle, corresponding to the system shown in Fig. 2. The red curve shows the wrapped angle, and the blue curve shows the unwrapped angle. The total accumulated orientation change is 1140 degrees over 2 s. (b) Trajectories of the centroids of the tube (red) and the droplet (blue) in the *x*,*y*-plane, both starting at the lower end points. The trajectory of the droplet's centroid has a length of 3.93 mm.

foams[37] and, in the case of silica particles, for air bubbles at planar water–air interfaces.[38]

The striking increase of the typical bubble size allows the tube to change from a spinning to an orbital motion that advances the tube tangentially along a circular trajectory. During this rotation, the tube is effectively wedged between the external surface of the drop and the solution–oxygen interface of the trapped bubble. An example is shown in Fig. 5 where the (here clockwise) rotation is easily discerned in the second row of panels. The rotation period is comparable to the period of spinning tubes. Notice that the transition from spinning to orbital motion is not abrupt but rather described by a continuous increase in the distance between the rotation center and the tube.

The bursting of large oxygen bubbles significantly perturbs the drop-tube system, typically repositioning the entire unit by up to 1 cm per burst. At first glance, such abrupt translational steps appear to violate linear momentum conservation. However, closer visual inspection reveals that each bubble-bursting event ejects several small satellite droplets at high speeds, each carrying momentum in various directions. Since the launch angles of these tiny droplets are erratic, their momentum sum typically does not cancel out, causing the droplet-tube system to recoil accordingly. An example for such a burst-induced repositioning step is shown in Fig. 5. Between the first and second panels of the third row (time marks 3.7 s and 3.8 s), the droplet decreases in size, inducing 0.3 s of movement in the 4 o'clock direction. Although the surface is superhydrophobic, residual friction gradually slows and eventually halts the droplet's translational motion.

Following the same image processing and analysis steps described for Fig. 3, Fig. 6 shows the temporal evolution of (a) the unwrapped tube axis angle and (b) the centroid coordinates of the tube as well as the solution drop. The largely increased time interval reveals that the sense of tube rotation changes five times during the experiment. The first directional change occurs 18 s into the experiment, switching the sense of rotation from clockwise to counter-clockwise. As a consequence, the

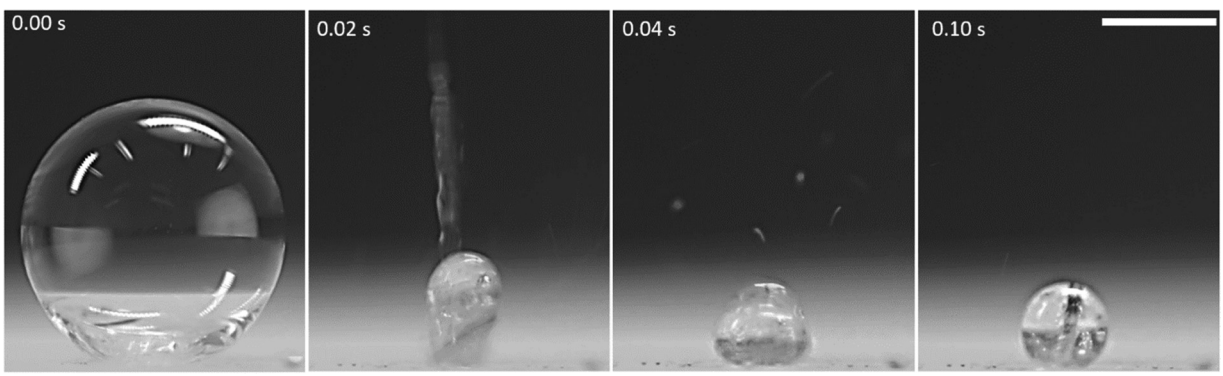

Fig. 4 Side views of an H_2O_2 drop with a chemical garden tube undergoing a bubble burst event. Initially the drop is inflated by a very large internal oxygen gas bubble forcing the buoyant tube into the lower portion of the drop. At around t = 0.02 s, the bubble is bursting and the drop is ejecting solution. By t = 0.10 s, the drop has returned to a near spherical shape. Scale bar: 1 cm (applies to all four panels). A video of this experiment is available in the (ESI†).

 This journal is © The Royal Society of Chemistry 2025

Open Access Article. Published on 18 July 2025. Downloaded on 9/15/2025 10:13:04 AM.
This article is licensed under a Creative Commons Attribution 3.0 Unported Licence.

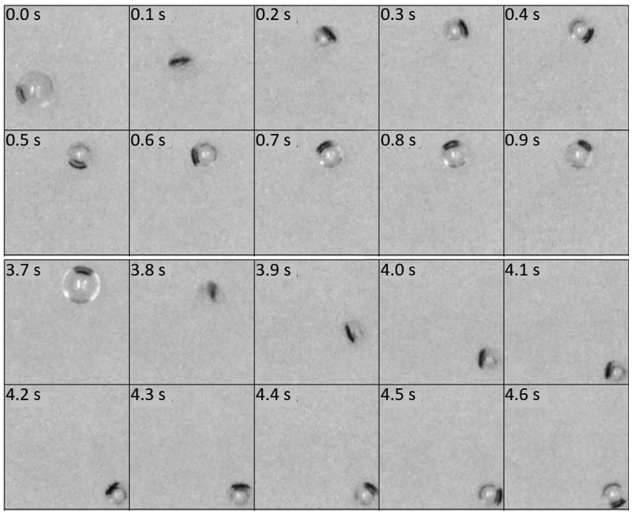

Fig. 5 Rotating motion of a chemical garden tube within a hydrogen peroxide droplet. The droplet also undergoes two consecutive translation events that follow gradual increases in the effective droplet volume. These motion steps are triggered by the sudden release of accumulated gas. The field of view is 1.4 × 1.4 cm^2 and the time interval between consecutive snapshots is 0.1 s with one larger time step between frames 10 and 11. The initial drop volume and H_2O_2 concentration are 10 μL and 15% v/v, respectively. A video of this experiment is available in the (ESI†).

angle θ that had increased to about 140 rad (800 deg), decreases for a few seconds until the next directional change reestablishes clockwise rotation and increasing values of θ. Notice that the difference between spinning and rotating motion is not resolved in this graph. Visual inspection shows the transition occurs around t = 10 s.

Orbital tube rotation clearly manifests in the trajectory of its centroid which describes circles with diameters comparable to the drop diameter. Eight or nine of these circles are discernible in Fig. 6 (red curve). The centroid of the drop (blue curve) follows a simpler trajectory and remains essentially stationary during the rotating-tube phases. In this experiment, the drop centroid moved a total of 99.3 mm while staying confined in a square of about 2 × 2 cm^2. The observed motion is reminiscent of the run-and-tumble dynamics of certain bacteria, which might suggest possible modeling strategies.[39]

Fig. 7 completes our example analysis by showing the drop's projected top-view area and its instantaneous speed over time. In panel (a), the cyan trace is the raw area extracted *via* our image-processing routine, and the black curve is the same data after median filtering to suppress noise. Over the course of the experiment the area varies between 5 to 20 mm^2, equivalent to a twofold change in the drop's apparent radius. Notice that the long, continuous area increase between t = 50 to 80 s has a decreasing slope as expected for a spherical bubble steadily growing inside the liquid drop. With a constant volumetric gas production rate k and disregarding curvature-related pressure changes, the area values A (50 s) = 6 mm^2 and A (80 s) = 15 mm^2 yield an estimate of $k \approx 1$ mm^3 s^{-1}. For comparison, very different, earlier measurements reported 0.1 mm^3 s^{-1} for 3% v/v rather than 15% v/v H_2O_2.[19]

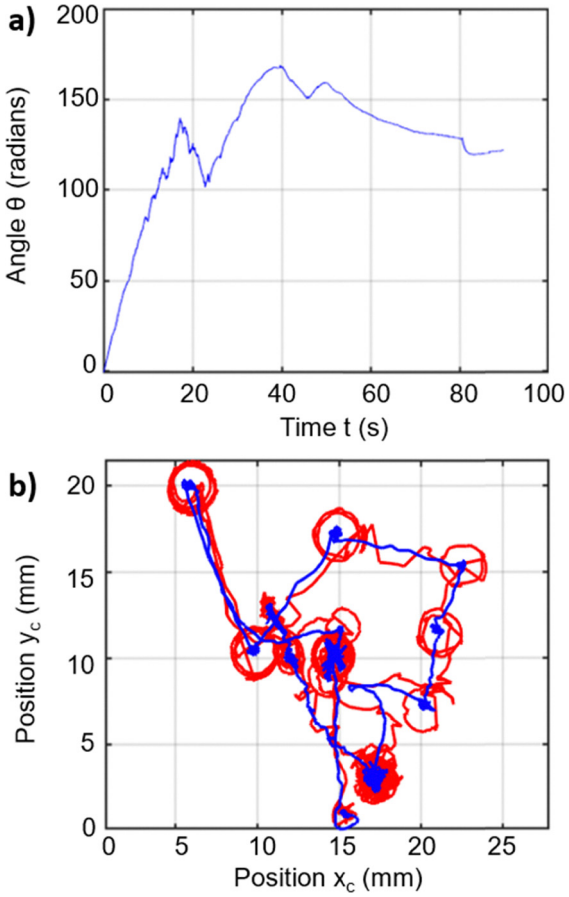

Fig. 6 Long-term rotational and translational dynamics of a chemical garden tube-droplet system. (a) Cumulative unwrapped orientation angle of the tube over the full active duration of the experiment (t_{active} = 90 s), including the events shown in Fig. 2, 3, and 5. (b) Trajectories of the centroids of the droplet (blue) and the tube (red) in the x,y-plane. The droplet undergoes a total translational displacement of approximately 99.3 mm. The tube's trajectory reflects its coupled rotational and translational motion throughout the experiment.

Panel (b) shows the drop speed evolution in the same experiment. Most of the time, the drop remains stationary but occasionally its speed bursts to values of 5–8 mm s^{-1}. These motion events last for about 2 s and coincide with abrupt decreases in drop area (marked by dashed lines). However, the relationship between the magnitude of the area change and the resulting speed is not strictly deterministic. It is rather influenced by the complex nature of the bursting events and possibly local variations in the surface. We note that the latter may include changes caused by prolonged contact between the solution drop and the substrate. Specifically, regions where the drop stays longer often develop a faint white haze which typically fades spontaneously within a few seconds after drop departure. From the motion patterns of the droplets, we observed no irreversible changes or hysteresis that could manifest as drop pinning. However, earlier studies reported continuous changes of contact angles and even the breakdown of superhydrophobicity over longer time scales of several minutes.[40,41]

Open Access Article. Published on 18 July 2025. Downloaded on 9/15/2025 10:13:04 AM.
This article is licensed under a Creative Commons Attribution 3.0 Unported Licence.

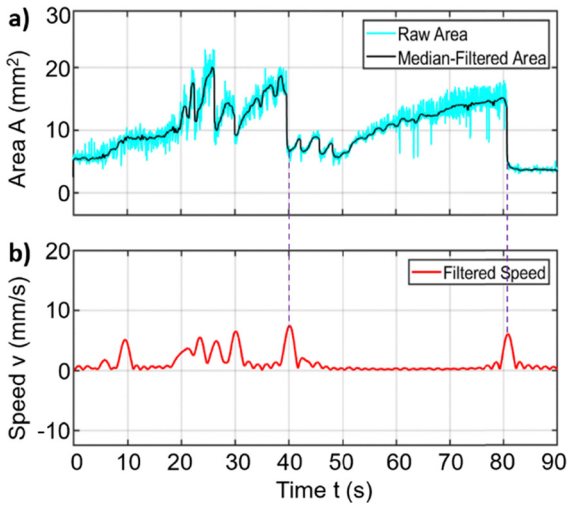

Fig. 7 Temporal evolution of the droplet's area and the centroid's speed throughout the active duration of the experiment. (a) Changes in the droplet's apparent cross-sectional area (viewed from above) show repeated expansion and sudden contraction episodes, corresponding to gas accumulation and release. (b) Peaks in the instantaneous speed of the droplet's centroid coincide with abrupt drops in area (highlighted by purple dashed lines), indicating that the translational motion is primarily driven by sudden gas release events.

3.3 Concentration dependencies

Lastly, we examine the effect of H_2O_2 concentration on the dynamics of the drop-tube units. Fig. 8 presents an analysis of four key observables across concentrations ranging from 0.5% to 15% v/v. Each data point represents the average of five independent experiments, and the error bars indicate the corresponding standard deviations.

Panel (a) shows the total travel distance of the drop. This distance remains near zero for concentrations below 3% v/v, indicating an absence of motion events. At higher concentrations, however, the total distance increases and approaches 6 cm, equivalent to more than 40 times the initial drop radius. As shown in panel (b), this trend is mirrored by the maximal drop speed, which also increases with H_2O_2 concentration.

Panel (c) analyzes internal activity by plotting the total accumulated angular change, $\sum|\Delta\theta|$. This measure increases nearly linearly with concentration, ultimately exceeding 80 full rotations. This finding can be understood in terms of an earlier study that reported a linear increase in the frequency of propulsion-bubble generation with increasing fuel concentration.[19] Moreover, panel (d) reveals that the lifetime of the dynamics decreases by over 50% as the H_2O_2 concentration increases. Here, we define the plotted active lifetime of the system as the time interval during which either the drop or the tube exhibit motion. The observed decrease is likely due to more pronounced fuel loss during bubble bursting and spray. It is interesting that these effects outcompete the increased concentration of the peroxide "fuel". Lastly, the data in (d) also explain that the increase in speed with concentration is less pronounced than the increase in distance.

4. Conclusions

In summary, we have demonstrated a novel form of active matter where a catalytic chemical garden tube enclosed within a small hydrogen peroxide droplet exhibits complex motility on superhydrophobic surfaces. The system displays spinning, rotating, and translational behaviors driven by asymmetric bubble detachment and repeated bursting events. These dynamics enable centimeter-scale displacements.

The observed droplet-tube behavior shares intriguing parallels with biological motility, especially through the internal localization of chemical fuel. Unlike systems driven by externally maintained gradients or bulk fuel reservoirs, our internalized propulsion provides a closer analogy to autonomous living cells that metabolize internal energy stores for motion. While the underlying physical mechanisms differ fundamentally from biological processes, our droplet-tube system opens new pathways toward synthetic active matter exhibiting increasing functional autonomy. Additionally, multi-unit interactions might be realized *via* vapor-mediated coupling between droplets, akin to the long-range attraction and chasing reported by Cira *et al.* in two-component propylene glycol–water droplets.[42,43] Lastly, we emphasize that the coupling of tube-drop motion could also be studied for H_2O_2-containing self-organizing reactions such as self-propelled Briggs–Rauscher droplets.[44]

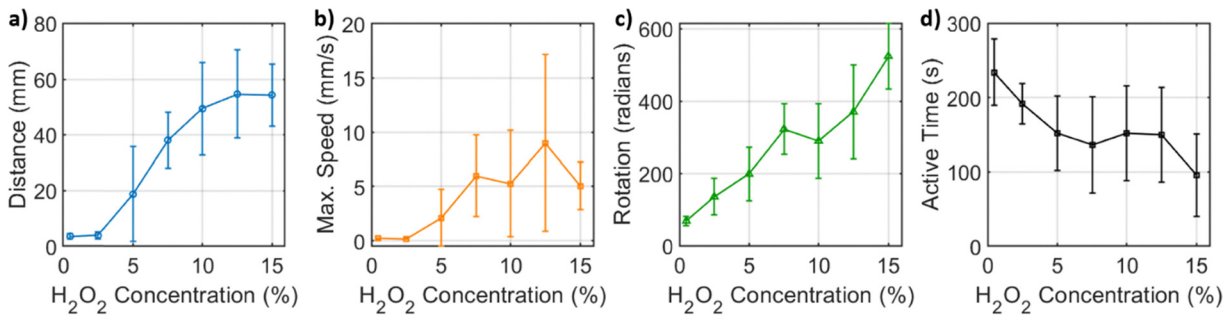

Fig. 8 Effect of hydrogen peroxide concentration (% v/v) on the dynamics of self-propelling tube-droplet cells. (a) and (b) Total distance and maximal instantaneous speed of the droplet during the system's active period. (c) Cumulative absolute angular change of the tube axis during spinning and rotation. (d) Active time, defined as the period during which either the droplet or the tube exhibits motion.

 This journal is © The Royal Society of Chemistry 2025

Open Access Article. Published on 18 July 2025. Downloaded on 9/15/2025 10:13:04 AM. This article is licensed under a Creative Commons Attribution 3.0 Unported Licence.

Overall, our work contributes to the growing exploration of soft, chemically driven locomotion by integrating catalytic activity, confined geometry, and surface interactions. Future research should investigate the fluid motion within the droplet, the influence of the tube material, and collective multi-drop as well as multi-tube behaviors to further approximate biological complexity and possibly achieve programmable autonomous functionality.

Author contributions

A. S. V.: conceptualization, methodology, investigation, formal analysis, writing; O. S.: conceptualization, formal analysis, resources, supervision, writing.

Conflicts of interest

There are no conflicts to declare.

Data availability

The data that support the findings of this study are available within the article. ESI† Movies are available at **https://github.com/osteinbock/TubeDropCell**.

Acknowledgements

This material is based on work supported by NASA under grant no. 80NSSC23M0050.

References

1 D. J. DeRosier, *Cell*, 1998, **93**, 17–20, DOI: **10.1016/S0092-8674(00)81141-1**.
2 M. Schliwa and G. Woehlke, *Nature*, 2003, **422**, 759–765, DOI: **10.1038/nature01601**.
3 R. D. Vale and R. A. Milligan, *Science*, 2000, **288**, 88–95, DOI: **10.1126/science.288.5463.88**.
4 E. Flaum and M. Prakash, *Science*, 2024, **384**, eadk5511, DOI: **10.1126/science.adk5511**.
5 H. Hess, G. D. Bachand and V. Vogel, *Chem. – Eur. J.*, 2004, **10**, 2110–2116, DOI: **10.1002/chem.200305712**.
6 S. Sanchez and M. Pumera, *Chem. – Asian J.*, 2009, **4**, 1402–1410, DOI: **10.1002/asia.200900143**.
7 M. G. van den Heuvel and C. Dekker, *Science*, 2007, **317**, 333–336, DOI: **10.1126/science.1139570**.
8 M. Tang, J. Ni, Z. Yue, T. Sun, C. Chen, X. Ma and L. Wang, *Angew. Chem., Int. Ed.*, 2024, **63**, e202315031, DOI: **10.1002/anie.202315031**.
9 H. Kitahata, N. Yoshinaga, K. H. Nagai and Y. Sumino, *Phys. Rev. E: Stat., Nonlinear, Soft Matter Phys.*, 2011, **84**, 015101, DOI: **10.1103/PhysRevE.84.015101**.
10 W. Gao, M. D'Agostino, V. Garcia-Gradilla, J. Orozco and J. Wang, *Small*, 2013, **9**, 467–471, DOI: **10.1002/smll.201201864**.
11 J. G. Gibbs and Y. P. Zhao, *Appl. Phys. Lett.*, 2009, **94**, 163104, DOI: **10.1063/1.3122346**.
12 L. Baraban, D. Makarov, R. Streubel, I. Mönch, D. Grimm, S. Sanchez and O. G. Schmidt, *ACS Nano*, 2012, **6**, 3383–3389, DOI: **10.1021/nn300413p**.
13 W. F. Paxton, K. C. Kistler, C. C. Olmeda, A. Sen, S. K. Angelo, Y. Cao, T. E. Mallouk, P. E. Lammert and V. H. Crespi, *J. Am. Chem. Soc.*, 2004, **126**, 13424–13431, DOI: **10.1021/ja047697z**.
14 W. Gao, S. Sattayasamitsathit, J. Orozco and J. Wang, *J. Am. Chem. Soc.*, 2011, **133**, 11862–11864, DOI: **10.1021/ja203773g**.
15 T. Mirkovic, N. S. Zacharia, G. D. Scholes and G. A. Ozin, *Small*, 2010, **6**, 159–167, DOI: **10.1002/smll.200901340**.
16 W. Zhu, P. Knoll and O. Steinbock, *J. Phys. Chem. Lett.*, 2024, **15**, 5476–5487, DOI: **10.1021/acs.jpclett.4c01031**.
17 J. Sun, R. Chu, X. Wu, Q. Yu, W. Xiao, H. Ao, Y. Wang, T. Wu, H. Ju, J. Wu and J. Lei, *J. Am. Chem. Soc.*, 2025, **147**, 17936–17945, DOI: **10.1021/jacs.5c02949**.
18 J. Li, I. Rozen and J. Wang, *ACS Nano*, 2016, **10**, 5619–5634, DOI: **10.1021/acsnano.6b02518**.
19 Q. Wang, P. Knoll and O. Steinbock, *J. Phys. Chem. B*, 2021, **125**, 13908–13915, DOI: **10.1021/acs.jpcb.1c09088**.
20 L. M. Barge, S. S. S. Cardoso, J. H. E. Cartwright, G. J. T. Cooper, L. Cronin, A. De Wit, I. J. Doloboff, B. Escribano, R. E. Goldstein, F. Haudin, D. E. H. Jones, A. L. Mackay, J. Maselko, J. J. Pagano, J. Pantaleone, M. J. Russell, C. I. Sainz-Díaz, O. Steinbock, D. A. Stone, Y. Tanimoto and N. L. Thomas, *Chem. Rev.*, 2015, **115**, 8652–8703, DOI: **10.1021/acs.chemrev.5b00014**.
21 B. C. Batista, A. Z. Morris and O. Steinbock, *Proc. Natl. Acad. Sci. U. S. A.*, 2023, **120**, e2305172120, DOI: **10.1073/pnas.2305172120**.
22 P. Knoll and C. C. Loron, *ChemSystemsChem*, 2024, **6**, e202400012, DOI: **10.1002/syst.202400012**.
23 S. Thouvenel-Romans, W. van Saarloos and O. Steinbock, *Europhys. Lett.*, 2004, **67**, 42–48, DOI: **10.1209/epl/i2003-10279-7**.
24 P. Knoll, A. V. Gonzalez, Z. C. McQueen and O. Steinbock, *Chem. – Eur. J.*, 2019, **25**, 13885–13889, DOI: **10.1002/chem.201903951**.
25 B. C. Batista, P. Cruz and O. Steinbock, *Langmuir*, 2014, **30**, 9123–9129, DOI: **10.1021/la5020175**.
26 M. Emmanuel, E. Lantos, D. Horváth and Á. Tóth, *Soft Matter*, 2022, **18**, 1731–1736, DOI: **10.1039/D1SM01808F**.
27 E. Balog, K. Bene and G. Schuszter, *Sci. Rep.*, 2025, **15**, 13241, DOI: **10.1038/s41598-025-97630-y**.
28 F. Glaab, J. Rieder, J. M. García-Ruiz, W. Kunz and M. Kellermeier, *Phys. Chem. Chem. Phys.*, 2016, **18**, 24850–24858, DOI: **10.1039/C6CP02107G**.
29 Q. Wang and O. Steinbock, *Soft Matter*, 2023, **19**, 2138–2145, DOI: **10.1039/D2SM01681H**.
30 P. Kumar, Q. Wang, D. Horváth, Á. Tóth and O. Steinbock, *Soft Matter*, 2022, **18**, 4389–4395, DOI: **10.1039/D2SM00395C**.
31 Q. Wang and O. Steinbock, *Phys. Chem. Chem. Phys.*, 2022, **24**, 14538–14544, DOI: **10.1039/D2CP01807A**.

Open Access Article. Published on 18 July 2025. Downloaded on 9/15/2025 10:13:04 AM.
This article is licensed under a Creative Commons Attribution 3.0 Unported Licence.

32 E. Evans, *Biophys. J.*, 1993, **64**, 1306–1322, DOI: **10.1016/S0006-3495(93)81497-8**.
33 N. Ecker and K. Kruse, *PLoS One*, 2021, **16**, e0246311, DOI: **10.1371/journal.pone.0246311**.
34 X.-M. Li, D. Reinhoudt and M. Crego-Calama, *Chem. Soc. Rev.*, 2007, **36**, 1350–1368, DOI: **10.1039/B602486F**.
35 E. A. Siev, B. C. Batista and O. Steinbock, *J. Phys. Chem. B*, 2024, **128**, 2028–2036, DOI: **10.1021/acs.jpcb.3c07840**.
36 D. Bleecher, P. Harsh, M. Hurley, A. K. Jones, R. Ross, V. K. Sikka and D. Zielke, *Highly durable superhydrophobic, oleophobic and anti-icing coatings and methods and compositions for their preparation*, *US Pat.*, 9067821B2, 2015.
37 J. Sun, L. Dai, K. Lv, Z. Wen, Y. Li, D. Yang, H. Yan, X. Liu, C. Liu and M.-C. Li, *Adv. Colloid Interface Sci.*, 2024, **328**, 103177, DOI: **10.1016/j.cis.2024.103177**.
38 Z. Du, M. P. Bilbao-Montoya, B. P. Binks, E. Dickinson, R. Ettelaie and B. S. Murray, *Langmuir*, 2003, **19**, 3106–3108, DOI: **10.1021/la034042n**.
39 A. Villa-Torrealba, C. Chávez-Raby, P. de Castro and R. Soto, *Phys. Rev. E*, 2020, **101**, 062607, DOI: **10.1103/PhysRevE.101.062607**.
40 P. Papadopoulos, L. Mammen, X. Deng and H.-J. Butt, *Proc. Natl. Acad. Sci. U. S. A.*, 2013, **110**, 3254–3258, DOI: **10.1073/pnas.1218673110**.
41 Y. Xiao, B. Li, C. Wei, A. Oron and Y. Jiang, *J. Colloid Interface Sci.*, 2025, **695**, 137810, DOI: **10.1016/j.jcis.2025.137810**.
42 N. J. Cira, A. Benusiglio and M. Prakash, *Nature*, 2015, **519**, 446–450, DOI: **10.1038/nature14272**.
43 H. Zhao, D. Orejon, K. Sefiane and M. E. R. Shanahan, *Langmuir*, 2025, **41**, 3986–3994, DOI: **10.1021/acs.langmuir.4c04255**.
44 M. Kuze, Y. Kubodera, H. Hashishita, M. Matsuo, H. Nishimori and S. Nakata, *ChemSystemsChem*, 2023, **5**, e202200030, DOI: **10.1002/syst.202200030**.

This journal is © The Royal Society of Chemistry 2025